



# Energy harvesting performance and flow structure of an oscillating hydrofoil with finite span



Daegyoun Kim<sup>a,b,\*</sup>, Benjamin Strom<sup>a,1</sup>, Shreyas Mandre<sup>a</sup>, Kenneth Breuer<sup>a</sup>

<sup>a</sup> School of Engineering, Brown University, Providence, 02912, USA

<sup>b</sup> Department of Mechanical Engineering, KAIST, Daejeon 34141, Republic of Korea

## ARTICLE INFO

### Keywords:

Tidal energy  
Hydrofoil  
Efficiency  
Leading-edge vortex

## ABSTRACT

The energy harvesting performance and resulting flow structures of a hydrofoil oscillating in pitch and heave are studied experimentally in a water flume. The shape of a hydrofoil cross-section is shown to have negligible influence on the power generation for the geometries tested. It is found that contribution to efficiency from heaving motion increases with reduced frequency at optimal pitching amplitude. However, contribution to efficiency from pitching motion decreases with reduced frequency because the development of a leading-edge vortex during the stroke is delayed at the high reduced frequency. Increasing the aspect ratio of the hydrofoil leads to a higher contribution to efficiency from heaving over the range of aspect ratios considered in this study. However, the effect of the aspect ratio on efficiency from pitching is negligible. When end plates are mounted at both ends of the hydrofoil, heaving power enhances. However, the enhancement of heaving power becomes smaller with increasing aspect ratio. Meanwhile, pitching power improves uniformly with the addition of end plates for all three aspect ratios. Our study suggests that the dependence of energy harvesting performance on aspect ratio is due to the delayed growth of the leading-edge vortex near the ends of the hydrofoil.

## 1. Introduction

Energy harvesting from flowing water such as ocean and tidal currents has emerged as a promising renewable energy resource, and research and development in this field is on the rise. Most of hydrokinetic energy harvesting technologies have been based on vertical-axis or horizontal-axis rotary turbines. As an alternative to rotary turbines, hydrokinetic energy harvesting using an oscillating hydrofoil has recently received increased attention, and some hydrofoil prototypes have been designed and tested (Kinsey et al., 2011; Young et al., 2014; Xiao and Zhu, 2014). Unlike horizontal-axis rotary turbines, which rely solely on steady force generation, the pitching and heaving hydrofoil employs an unsteady force generation mechanism (Kinsey and Dumas, 2008; Zhu and Peng, 2009). When the hydrofoil pitches up at a high angle of attack, a “dynamic stall” vortex is created at the leading-edge of the hydrofoil. Because of the low pressure on the upper suction surface created by the leading-edge vortex, the hydrofoil can generate a large heaving force. However, as the leading-edge vortex separates from the hydrofoil and moves downstream, the heaving force decreases quickly and in order to maximize power production, the hydrofoil should rotate, changing the sign of its pitch angle, and begin to heave in the opposite direction, creating another leading edge vortex. This periodic pitching and heaving motion can efficiently extract energy from the kinetic energy of a fluid flow and is also used as one of the unsteady propulsion mechanisms in the

\* Corresponding author at: Department of Mechanical Engineering, KAIST, Daejeon 34141, Republic of Korea.

E-mail address: [daegyoun@kaist.ac.kr](mailto:daegyoun@kaist.ac.kr) (D. Kim).

<sup>1</sup> Current address: Northwest National Marine Renewable Energy Center, University of Washington, Seattle 98195, USA.

Nomenclature			
$c$	Hydrofoil chord	$f$	Oscillation frequency
$s$	Hydrofoil span	$f^*$	Reduced frequency ( $fc/U_\infty$ )
$U_\infty$	Free-stream velocity	$T$	Oscillation period
$AR$	Aspect ratio ( $s/c$ )	$t^*$	Non-dimensional time ( $t/T$ )
$A_s$	Full swept area of the leading edge	$F$	Heaving force
$d$	Distance from the hydrofoil to the edge of the end plate	$M$	Pitching torque
$h$	Heaving position	$C_F$	Heaving force coefficient ( $2F/\rho U_\infty^2 A_s$ )
$h_0$	Heaving amplitude	$C_M$	Pitching torque coefficient ( $2M/\rho U_\infty^2 c A_s$ )
$\theta$	Pitching angle	$P$	Power ( $Fh + M\theta$ )
$\theta_0$	Pitching amplitude	$\eta$	Total efficiency ( $2\bar{P}/\rho U_\infty^3 A_s$ )
$\alpha_e$	Effective angle of attack	$\eta_h$	Heaving efficiency ( $2\bar{F}h/\rho U_\infty^3 A_s$ )
		$\eta_P$	Pitching efficiency ( $2\bar{M}\theta/\rho U_\infty^3 A_s$ )
		$\omega$	Spanwise vorticity
		$\Gamma_{nd}$	Non-dimensional circulation ( $\int \omega dA/U_\infty c$ )

flapping locomotion of animals (Maxworthy, 1979; Ellington, 1996).

The oscillating hydrofoil technology has several advantages over the conventional turbine technology (Xiao and Zhu, 2014). The maximum blade speed of the hydrofoil is several times lower than the blade tip speed of a conventional turbine at optimal operation, which may reduce harmful interactions with aquatic animals. In addition, the device is structurally more robust because it does not rely on the fast rotation of long blades. Since the hydrofoil can be designed to have a high aspect ratio, it is also advantageous in operation in shallow water channels where the velocity of tidal currents is high (Franck et al., 2015).

The study of energy extraction using flapping foils was pioneered by Birnbaum (1924). The analytical and experimental study of McKinney and DeLaurier (1981) showed that the flapping foil could extract energy and its efficiency was comparable to rotary turbines. In the last several years, researchers have investigated the relationship between operational parameters, resulting flow structures, and overall energy harvesting performance. Jones and Platzer (1997) numerically studied the pitching-only, heaving-only, and combined motions of the power-extracting foil over a broad parameter space. Simpson et al. (2008) conducted an experimental parametric study on the influence of the reduced frequency ( $f^* = fc/U_\infty$  where  $f$  is the operating frequency,  $U_\infty$ , the freestream velocity, and  $c$ , the hydrofoil chord), the maximum effective angle of attack ( $\alpha_e$ ) and the hydrofoil aspect ratio ( $AR = s/c$  where  $s$  is the hydrofoil span) on energy harvesting performance. Through a computational parametric study of the frequency and pitching amplitude domain, Kinsey and Dumas (2008) showed that energy conversion efficiency could be as high as 34%. By investigating the relationship between wake stability and efficiency, Zhu (2011) proposed a reduced frequency,  $f^*$ , of about 0.15 for optimal performance. With a passive heaving motion induced by an imposed pitching motion, high efficiency was achieved by controlling the interaction between the flapping foil and the leading-edge vortex (Zhu and Peng, 2009).

In order to improve energy extracting performance of the oscillating foil, several ideas have been proposed. It has been reported that efficiency increased when a trapezoid-like pitching motion with a sinusoidal heaving motion was used instead of sinusoidal pitching and heaving motions (Ashraf et al., 2011; Xiao et al., 2012). A corrugated foil inspired by a scallop shell enhanced efficiency by 6% as compared to the NACA0012 foil in the same conditions (Le et al., 2013). When the foil was placed either near a solid wall or between two parallel plane walls, it generated more power than the foil in an unconfined flow (Wu et al., 2014). A flexible foil could enhance efficiency by increasing the peaks in lift force over a flapping cycle (Liu et al., 2013). The foil with a deformable tail also improved efficiency compared to a foil with a rigid tail (Wu et al., 2015). It was also found that, in a streamwise tandem configuration of the foils, favorable interaction between the downstream foil and the wake vortices could lead to high power extraction (Kinsey and Dumas, 2012a). Energy harvesting for the tandem configurations was also studied experimentally and computationally by Fenercioglu et al. (2015a) and Karakas and Fenercioglu (2016). In addition, by placing side walls, the foil in confined flow could outperform the highest efficiency case in free flow (Karakas et al., 2016).

Despite the extensive reports regarding energy harvesting hydrofoils, most of the studies have been conducted using two-dimensional numerical simulations, and there have been few studies on the three-dimensional effects of a hydrofoil with finite span in spite of its importance in practical applications. The experimental work of Simpson et al. showed that the efficiency of the foil increased with aspect ratio (Simpson et al., 2008). The computational work of Kinsey and Dumas found that, compared to its 2D equivalent, average power extracted from a three-dimensional foil dropped by 20%–30%, and the end plates attached to both ends of the hydrofoil could recover some of this loss (Kinsey and Dumas, 2012b). However, these studies focused solely on the efficiency trends with different aspect ratios rather than providing any detailed analysis on the leading-edge vortex dynamics and its relation to hydrofoil performance.

Most, if not all, of the previous studies have considered airfoil-derived geometries such as the NACA0012. The use of flat plates instead of airfoils was first introduced by Semler (2010) and Platzer et al. (2011). Given that the key to oscillating hydrofoil performance is the formation and capture of a strong leading-edge vortex, one might suspect that a classically shaped airfoil, which is designed to mitigate separation effects, may not necessarily be optimal and is certainly unlikely to be required. Furthermore, a simple geometry would be extremely attractive from the perspective of manufacturing and maintenance costs associated with an energy harvesting system. For this reason, it is desirable to closely examine the effect of various hydrofoil cross-section geometries on device performance, with a focus on the leading-edge shape.

With these issues in mind, the present work extends this body of literature in several important ways. Firstly, we provide much

needed experimental data with a lab-scale hydrofoil by conducting force measurements and quantitative flow measurements. We conducted a parametric study over a broad range of pitching amplitudes, heaving amplitudes, and frequencies. In addition, the effect of the hydrofoil shape on the system performance was examined. As part of this analysis, we analyze the pitching motion and heaving motion separately and describe how these two components contribute to the overall energy extraction efficiency. Most importantly, we correlate these trends with Particle Image Velocimetry (PIV) measurements of the leading-edge vortex dynamics. Finally, we examine the effect of the hydrofoil's aspect ratio and the use of end plates on the leading-edge vortex structure and the energy harvesting efficiency.

## 2. Experimental setup

Experiments were conducted in a free-surface water flume at Brown University. The test section of the water tunnel was 80 cm wide and 57 cm deep. The hydrofoil model was vertical, suspended from a carriage located above the water line (Fig. 1a). Several cross-sectional shapes of the hydrofoil were considered in this study. We mainly used a hydrofoil with an elliptical or rectangular cross section (chord,  $c$ , of 10 cm and thickness of 1 cm) and with the pitch axis located at the half-chord (Fig. 1b). The symmetric geometry was chosen because of our primary application: bi-directional tidal flows. Other geometries are discussed in Section 3.1.

The hydrofoil was actuated by a linear motor (I-FORCE ironless motor, Parker) for heaving motion and by a rotary stepper motor (ST5-Q-NE, Applied Motion Products) for pitching motion (Fig. 1b). Optical encoders provided position measurements and feedback for both degrees of freedom. In this work, passive pitching or heaving motion induced by the free stream was not considered. Pitch angle  $\theta$  was controlled by a controller of Electro Standards Laboratories, and heaving displacement  $h$  was controlled by a controller of Advanced Motion Controls. Pitching and heaving kinematics were scripted in MATLAB and kinematics signals were sent to the control softwares using a DAQ board (PCIe-6351, National Instruments). Both motions were sinusoidal:

$$\theta(t) = -\theta_0 \cos(2\pi ft + \pi/2) \quad \text{and} \quad h(t) = -h_0 \cos(2\pi ft), \tag{1}$$

where  $\theta_0$  and  $h_0$  are pitching and heaving amplitudes, respectively.  $f$  is frequency, and  $t$  is time. Even though not considered in this study, it was reported that non-sinusoidal pitch angle profiles produced the better efficiency than sinusoidal pitch angle profiles (Young et al., 2013; Fenercioglu et al., 2015b). Reduced frequency  $f^* (=fc/U_\infty)$  was varied from 0.08 to 0.20 for 13 different values in about 0.01 increment, and pitching amplitude  $\theta_0$  was varied from  $45^\circ$  to  $85^\circ$  for nine different values in  $5^\circ$  increment. Non-dimensional heaving amplitude  $h_0^* (=h_0/c)$  was varied from 0.5 to 1.0 for six different values in 0.1 increment.

The pitching torque  $M$  acting on the hydrofoil was measured with a reaction torque sensor (TFF400, Futek) while the heaving force  $F$ , was measured with a load cell (LCM300, Futek). The torque sensor and load cell data were recorded using the DAQ board at 1 kHz. Both torque sensor and load cell were calibrated with the hydrofoil device. In order to isolate fluid forces from mechanical friction loss and inertial force and torque due to the acceleration of the hydrofoil, we repeated the experiments in still air, and subtracted the measurements of the pitching torque and heaving force from those obtained in the water flow. By doing so, only hydrodynamic force and torque were considered in the evaluation of power and efficiency. The measurement of the pitching torque and heaving force is repeated five times for the same case, and, for all cases, the standard deviations of pitching torque and heaving force are within 6% and 4% of the mean values, respectively.

The instantaneous power,  $P$ , and efficiency,  $\eta$ , were defined as

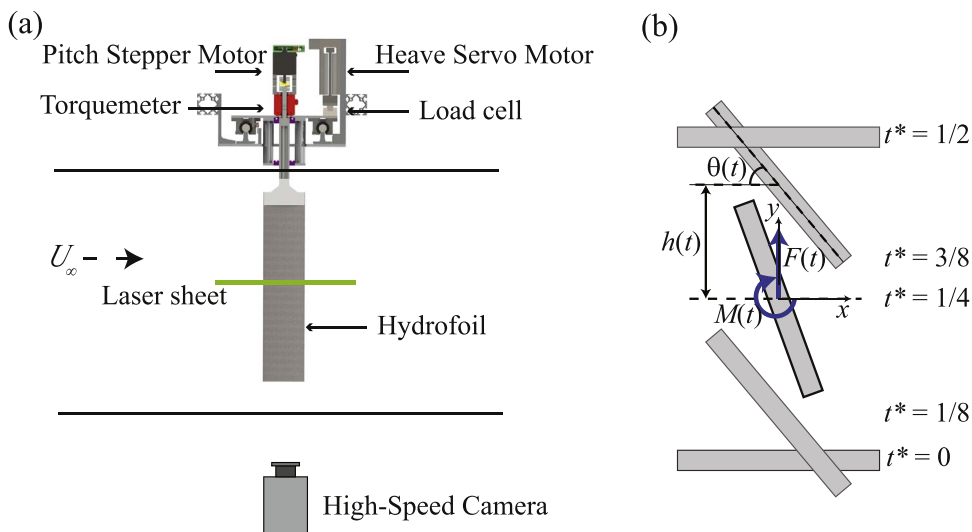


Fig. 1. (a) Schematic of the hydrofoil installed in the water flume. (b) Pitching and heaving motions of the hydrofoil in top-down view. For clarity, only one half of the stroke cycle is shown.  $T$  is the period of a cycle, and  $t^* (=t/T)$  is dimensionless time.

$$P(t) = F(t)\dot{h}(t) + M(t)\dot{\theta}(t) \quad \text{and} \quad \eta = \frac{2\overline{P(t)}}{\rho U_\infty^3 A_s}, \tag{2}$$

where  $\overline{P(t)}$  is the cycle-averaged power, and  $A_s$  is the swept area of the hydrofoil - the maximum transverse excursion of the leading edge multiplied by the span. A list of the main parameters used in this study is presented in the appendix.

The free-stream speed,  $U_\infty$ , measured in the center of the test section was 0.503 m/s with standard deviation 0.006 m/s, and the Reynolds number ( $=U_\infty c/\nu$ ) based on the chord and the free-stream speed was  $5.0 \times 10^4$ . Three hydrofoil spans,  $s=25$  cm, 35 cm, and 45 cm were used to obtain three aspect ratios  $AR(=s/c)$ , 2.5, 3.5, and 4.5. In any tunnel experiment, the blockage effects due to the flume side walls should be taken into consideration. Unfortunately, there is no reliable empirical correction about the blockage effect for a model that continues to change its position and frontal area in a tunnel experiment. The ratio of the hydrofoil area  $sc$  to the test section area is 5% for the  $AR=2.5$  hydrofoil and 10% for the  $AR=4.5$  hydrofoil. Actual frontal area of the hydrofoil changes due to the pitching motion. The mean ratio of the actual frontal area to the test section during the stroke is 4% for  $AR=2.5$  and 7% for  $AR=4.5$  for the maximum pitch amplitude case,  $\theta_0 = 85^\circ$ , which may be small enough to neglect the blockage effect. Other related experiments with a smaller chord,  $c=7.5$  cm, have yielded results indistinguishable from those presented here, and thus the blockage effect is assumed to be negligible. In order to reduce three-dimensional tip flow near both ends of the hydrofoil, end plates were also mounted at both ends (Fig. 2a). Four different sizes of the end plates were considered to evaluate the size effect on the hydrofoil performance; the distance from the hydrofoil to the edge of the end plates  $d$  was  $0.25c$ ,  $0.50c$ ,  $0.75c$ , and  $1.00c$  (Fig. 2b).

Planar particle image velocimetry (PIV) was used to measure the velocity field around the hydrofoil (Fig. 1a). Two cameras (1024×1024 pixels, FASTCAM SA3, Photron) were mounted below the test section, facing upwards. The cameras were placed side by side in order to expand the field of view in the heaving direction. The tunnel was seeded with silver-coated hollow ceramic spheres of 70 μm (AG-SL150-16-TRD, Potters Industries). The particles were illuminated by a horizontal Nd:YLF laser sheet (30 mJ/pulse, DM30-527, Photonics Industries) located at three different spanwise positions of the vertical hydrofoil; one laser plane was positioned at the middle of the hydrofoil span ( $z = z_0$ ;  $z/s = 0.5$ ), and two other laser planes located at  $z/s = 0.67$  and  $0.83$  (Fig. 2a). The cameras and the laser were triggered by the hydrofoil control system and synchronized with the hydrofoil motion. The time delay between two images of a pair was 2 ms. Image pairs were recorded at 25 Hz for 20 cycles and processed with DaVis software (LaVision). Each pair of the images was cross-correlated with a multi-grid interrogation scheme. The first interrogation window size was 128×128 pixels with a 50% overlap, and the final window size was 32×32 pixels with a 50% overlap. When the flow field at the middle of the hydrofoil ( $z = z_0$ ) was measured, the total field of view was 32 cm×49 cm, and the grid size of the velocity fields was 5.0 mm. Outlier vectors were removed and replaced by the interpolation of their surrounding neighbor vectors. The velocity fields were phase-averaged over 20 cycles. For a phase-averaged velocity field, the standard deviation of the velocity magnitude is within 5% of the maximum velocity magnitude for each time step. Vorticity fields were obtained from the velocity field by taking central finite difference scheme.

### 3. Results and discussion

#### 3.1. Energy harvesting performance of an oscillating hydrofoil

The efficiency,  $\eta$ , defined in Eq. (2) is obtained for a broad range of pitching amplitudes  $\theta_0$ , non-dimensional heaving amplitudes  $h_0^*$ , and reduced frequencies  $f^*$  for the hydrofoil with an elliptical cross section and aspect ratio,  $AR(=s/c) = 4.5$  (Fig. 3). In our study, the maximum efficiency  $\eta$  was 0.30 at  $f^* = 0.13$ ,  $\theta_0 = 70^\circ$ , and  $h_0^* = 0.8$ . This result agrees well with the results of previous studies; a numerical simulation of a two-dimensional hydrofoil showed that the maximum efficiency was about 34% at the optimal  $f^*$  of 0.15 (Kinsey and Dumas, 2008), and a corresponding experiment showed that the maximum efficiency reached 30% for  $f^*$  near 0.12 (Kinsey et al., 2011). In each subfigure of Fig. 3, one parameter was held constant at the value corresponding to the maximum efficiency. The efficiency does not increase or decrease monotonically with  $f^*$  or  $\theta_0$ , but has an optimal value in the middle of the parameter domain. In general, when the heaving amplitude increases from  $h_0^* = 0.5$  to 1.0, the power tends to increase. However, in

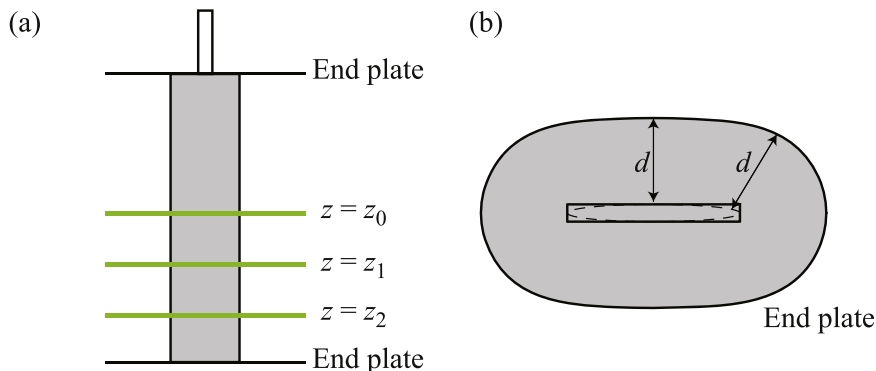
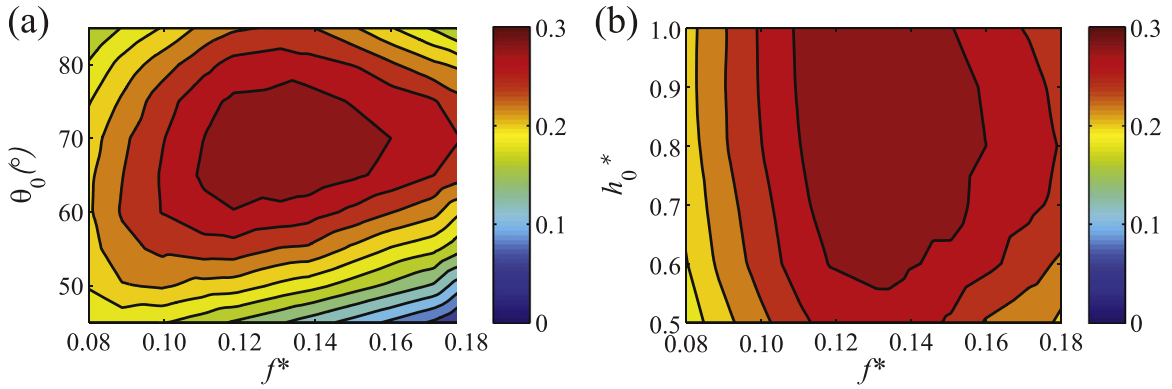


Fig. 2. (a) Side view and (b) top view of a hydrofoil with two end plates. Three green lines are the positions of a horizontal laser sheet.  $d$  is the distance from the hydrofoil to the edge of the end plate.



**Fig. 3.** Contours of efficiency  $\eta$ . (a) Heaving amplitude  $h_0^*$  is fixed as 0.8. (b) Pitching amplitude  $\theta_0$  is fixed as  $70^\circ$ . The aspect ratio of the hydrofoil is 4.5, and the cross-section of the hydrofoil is elliptical.

the efficiency definition (Eq. (2)), the denominator is the maximum frontal area which is closely related with the heaving amplitude, and the optimal efficiency is found near  $h_0^* = 0.8$ . As can be seen in Fig. 3b, the efficiency is comparatively less sensitive to the heaving amplitude. For each  $h_0^*$  tested in this study, the maximum efficiency is about 0.28 – 0.30, and the corresponding  $\theta_0$  and  $f^*$  are between  $65^\circ - 70^\circ$  and 0.13 – 0.14, respectively. For this reason, we will consider only  $h_0^* = 0.8$  case from now on.

One of the parameters relevant to energy extracting performance is the effective angle of attack,  $\alpha_e$ , defined below, which accounts for the heaving velocity  $\dot{h}$  of the hydrofoil (Fig. 4a):

$$\alpha_e(t) = \theta(t) - \tan^{-1}\left(\frac{\dot{h}(t)}{U_\infty}\right) \quad \text{and} \quad \alpha_{e,max} = \theta_0 - \tan^{-1}\left(\frac{2\pi fh_0}{U_\infty}\right). \tag{3}$$

In the sinusoidal heaving and pitching motions,  $\alpha_e$  is maximum in the middle of the stroke. Simpson et al. studied the relationship between efficiency  $\eta$  and maximum  $\alpha_e$ , and Kinsey and Dumas also found that the maximum  $\alpha_e$  was a more appropriate parameter for predicting the energy extraction regime than the pitching amplitude alone (Kinsey and Dumas, 2008; Simpson et al., 2008). Interestingly, for each value of  $f^*$ , the maximum  $\eta$  is found when the maximum  $\alpha_e$  is between  $30^\circ$  and  $40^\circ$ , although the scaling of the efficiency curves with  $\alpha_e$  does not hold at both high and low frequencies (Fig. 4b). Even though maximum  $\alpha_e$  cannot be used as the sole parameter to determine energy harvesting performance, this result indicates that optimization of maximum  $\alpha_e$  may be a simple approach to produce high efficiency  $\eta$  at a given  $f^*$ .

To explore the effects of foil and leading-edge geometries, we evaluated the hydrofoil performance for the cross-sections shown in Fig. 5. The five cross-section geometries tested were: an elliptical hydrofoil, a thick rectangular hydrofoil, a hydrofoil with rounded edges, a hydrofoil with beveled edges of  $90^\circ$  and a thin rectangular hydrofoil. The maximum thickness for all of the foils was 10% of the chord, except for the thin rectangular hydrofoil which had a maximum thickness of 5%. As shown in Fig. 5, the efficiency is not significantly influenced by the cross-section shape of the hydrofoil. The difference of maximum efficiency among the five cases lies within  $\eta = 0.02$ . In retrospect, this result is not surprising. A leading-edge vortex responsible for power generation of the hydrofoil is created by the roll-up of the separated shear layer at the leading edge. As long as separation occurs at the leading edge, the shape of the hydrofoil does not affect the growth of the leading-edge vortex. A similar result was reported by the computational study of Kinsey and Dumas who tested symmetric foils with 2, 15, and 20% thickness and found very little change in performance (Kinsey and Dumas, 2008). Usoh et al. (2012) and Usoh (2015) also computationally showed that the performance of a rectangular hydrofoil

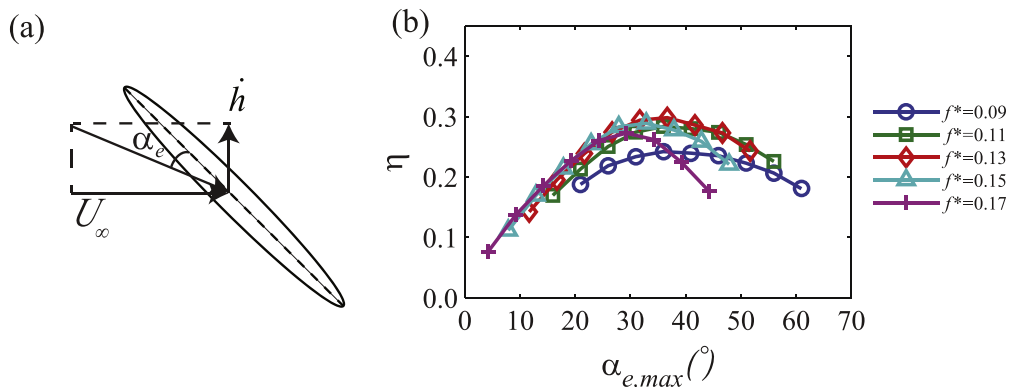


**Fig. 4.** (a) Definition of the effective angle of attack  $\alpha_e$ . (b) Relationship between efficiency by heaving  $\eta_h$ , and maximum effective angle of attack  $\alpha_e$  for five reduced frequencies  $f^*$ ;  $f^* = 0.09(\circ)$ ,  $0.11(\square)$ ,  $0.13(\diamond)$ ,  $0.15(\triangle)$ , and  $0.17(+)$ . The cross section of the hydrofoil is elliptical.

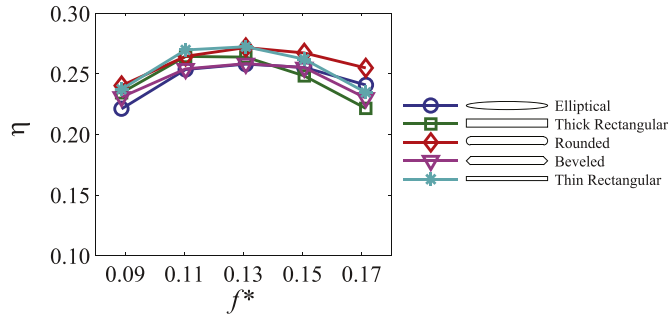


Fig. 5. Comparison of efficiency  $\eta$  for five different shapes of the cross section; the shapes are shown in the legend.  $\theta_0=70^\circ$  and  $h_0^*=0.8$ .

is 5.35% over that of the profiled counterpart, NACA0012. In a conventional horizontal-axis rotary turbine, which depends critically on the maintenance of attached flow, the optimization of blade cross section is very important, and small changes in the blade shape can change the performance significantly. In contrast, the fact that a wide variety of hydrofoil cross sections show similar performance provides a huge advantage in the design and manufacturing process of the oscillating hydrofoil system. Also, from this result, we can conjecture that the hydrofoil may be able to maintain its performance in unfavorable environmental conditions which might occur due to biofouling and corrosion. Given these results, for the following sections, we consider only a 10% thick rectangular hydrofoil.

3.2. Power due to the heaving motion

In order to further understand the relationship between the parameters and device performance, the total efficiency  $\eta$  is divided into two components, the efficiency contributed by heaving motion  $\eta_h$  and the efficiency contributed by pitching motion  $\eta_p$  for the hydrofoil with a rectangular cross section:

$$\eta_h = \frac{2\overline{F\dot{h}}}{\rho U_\infty^3 A_s} \quad \text{and} \quad \eta_p = \frac{2\overline{M\dot{\theta}}}{\rho U_\infty^3 A_s}. \tag{4}$$

Contours of the contribution to efficiency by heaving,  $\eta_h$ , are shown in Fig. 6a. In general,  $\eta_h$  tends to increase with  $f^*$  as long as  $\theta_0$  is high enough.  $\eta_h$  reaches its maximum at  $\theta_0 = 70^\circ$ , but continues to increase as  $f^*$  increases, in contrast to the total efficiency  $\eta$  which has an optimal value in the middle of the  $f^*$  domain considered in this study (Fig. 3a,  $\theta_0 = 70^\circ$  and  $f^* = 0.13$ ). At  $\theta_0 = 70^\circ$ ,  $\eta_h$  is 0.22 at  $f^* = 0.08$  and 0.41 at  $f^* = 0.18$ ; it increases almost linearly between  $f^* = 0.08$  and  $f^* = 0.18$ . Meanwhile, at  $\theta_0 = 50^\circ$ , the slope of  $\eta_h$  vs.  $f^*$  is negligible;  $\eta_h$  is 0.22 at  $f^* = 0.08$  and 0.21 at  $f^* = 0.18$ .

Figs. 7a and b show the phase-averaged heaving force coefficient  $C_F(t^*) (=2F/\rho U_\infty^2 A_s)$  and heaving efficiency  $\eta_h(t^*) (=2F\dot{h}/\rho U_\infty^3 A_s)$  for a fixed pitch amplitude,  $\theta_0 = 70^\circ$ , and three reduced frequencies,  $f^* = 0.09, 0.13,$  and  $0.17$ . Since heaving power is symmetric between upstroke and downstroke, the time histories of  $C_F$  and  $\eta_h$  are described only for the upstroke ( $0 \leq t^* (=t/T) \leq 0.5$ ). In the middle of the upstroke, the  $f^* = 0.17$  case generates the smallest heaving force  $F$  (Fig. 7a). Since the heaving velocity  $\dot{h}$  is proportional to the frequency,  $\dot{h} = 2\pi f h_0 \sin(2\pi f t)$  from Eq. (1), the larger reduced frequency case has a larger heaving velocity and a smaller effective angle of attack (see Eq. (3)). As a result, the component of the hydrodynamic force exerted on the hydrofoil in the heaving direction is reduced for the high reduced frequency case, and most of the hydrodynamic force is applied in the streamwise direction. However, since the power due to the heaving motion,  $F \cdot \dot{h}$ , is the product of the heaving force,  $F$ , and the heaving velocity,  $\dot{h}$ , which scales with  $f$  ( $\dot{h} \propto f$ ), the higher reduced frequency case can produce a larger heaving efficiency  $\eta_h$  despite generating a

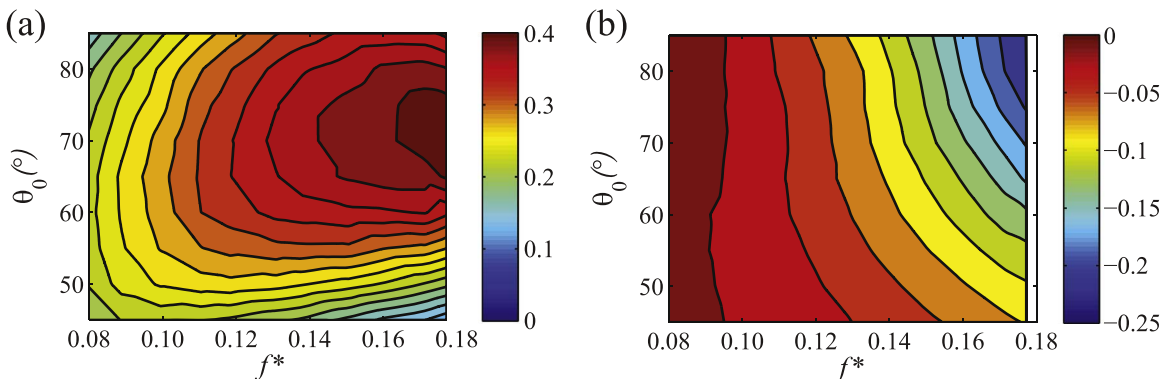
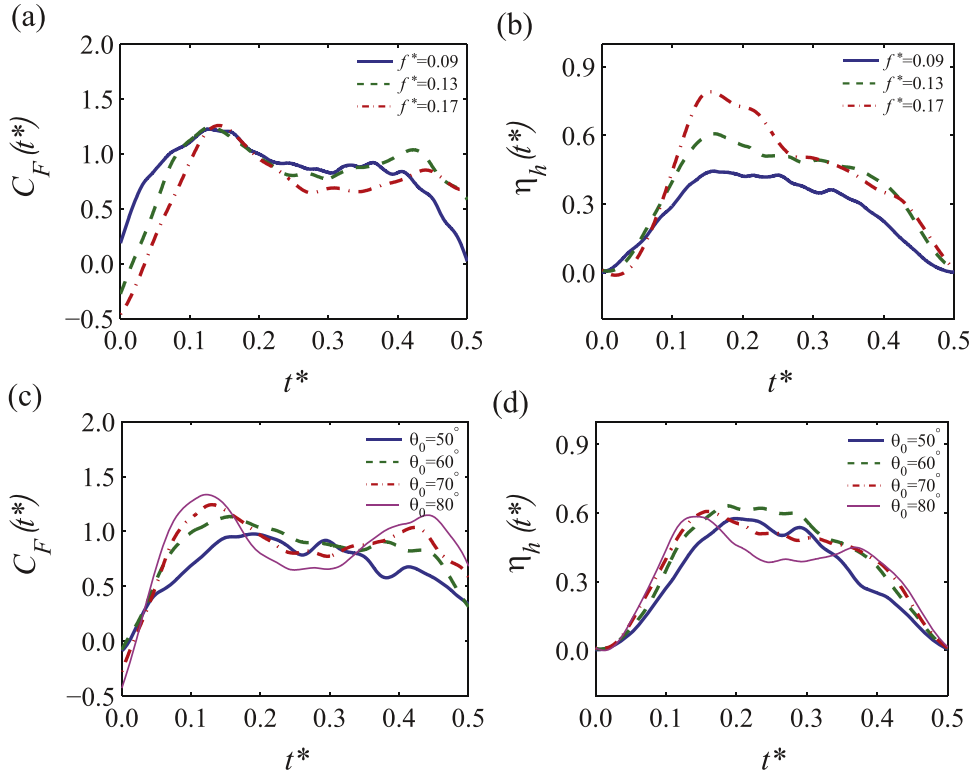


Fig. 6. Contours of (a) efficiency contributed by heaving motion  $\eta_h$ , and (b) efficiency contributed by pitching motion  $\eta_p$ , with respect to the pitching amplitude  $\theta_0$  and the reduced frequency  $f^*$ . The aspect ratio of the hydrofoil is 4.5, and  $h_0^*$  is 0.8. The cross section of the hydrofoil is rectangular with chord 10 cm and thickness 1 cm.



**Fig. 7.** Time histories of the heaving force coefficient  $C_F(t^*)$  ((a) and (c)) and efficiency due to heaving  $\eta_h(t^*)$  ((b) and (d)) during upstroke. (a) and (b):  $\theta_0 = 70^\circ$ . (c) and (d):  $f^* = 0.13$ . The cross-section of the hydrofoil is rectangular.

smaller heaving force (Fig. 7b);  $\eta_h$  is 0.25 at  $f^* = 0.09$ , 0.37 at  $f^* = 0.13$ , and 0.41 at  $f^* = 0.17$ .

For a given  $f^*$ ,  $\eta_h$  is maximum near  $\theta_0 = 60^\circ - 70^\circ$  and tends to decrease outside of that range (Fig. 6a). Figs. 7c and d show the time histories of  $C_F(t^*)$  and  $\eta_h(t^*)$  for four pitching amplitudes at  $f^* = 0.13$ . Since the frequency and heaving velocity are the same for the four cases, the difference in power generation is due to the variation in the heaving force. In the early and late phases of the upstroke, the larger  $\theta_0$  case generates the larger  $C_F(t^*)$  and  $\eta_h(t^*)$  (Figs. 7c and d). However, in the middle of the upstroke,  $C_F(t^*)$  and  $\eta_h(t^*)$  drop noticeably for  $\theta_0 = 80^\circ$ . Because of high pitch angle, the hydrodynamic force acting on the hydrofoil is mostly in the streamwise direction, and only a small component of the force is in the heaving direction. Because of the decrease in heaving force and heaving power in the middle of the stroke,  $\eta_h$  does not increase monotonically with  $\theta_0$  for the given  $f^*$ , but has a maximum value near  $\theta_0 = 60^\circ - 70^\circ$ .

### 3.3. Power due to the pitching motion

The contribution to the efficiency by pitching,  $\eta_p$ , obtained in Eq. (4), is presented in Fig. 6b for the hydrofoil with a rectangular cross section.  $\eta_p$  generally decreases with both pitching amplitude  $\theta_0$  and reduced frequency  $f^*$ . The efficiency due to pitching,  $\eta_p$ , is near zero when  $\theta_0$  and  $f^*$  are low, and it can be less than  $-0.20$  at the highest  $f^*$  and  $\theta_0$  considered in this work. Since pitching angular velocity  $\dot{\theta}$  is scaled with the product of  $\theta_0$  and  $f^*$  ( $\dot{\theta} = -2\pi f^* \theta_0 \sin(2\pi f^* t + \pi/2)$  from Eq. (1)), the trend that  $\eta_p$  changes monotonically with  $\theta_0$  and  $f^*$  may be expected. The question remains as to why  $\eta_p$  is near zero at low frequencies and becomes negative in high frequencies. For example, while  $\eta_p$  is just between  $-0.01$  and  $0$  in the range of  $\theta_0 = 45^\circ - 85^\circ$  at  $f^* = 0.09$ , it is between  $-0.19$  and  $-0.07$  at  $f^* = 0.17$ . In order to examine this dependence of  $\eta_p$  on  $f^*$  in more detail, the time histories of pitching torque coefficient  $C_M(t^*)$  defined as  $2M/\rho U_\infty^2 c A_s$ , are compared between the low reduced frequency  $f^* = 0.09$  and the high reduced frequency  $f^* = 0.17$  in Fig. 8.

At the low frequency,  $f^* = 0.09$ ,  $C_M(t^*)$  at the four different pitching amplitudes is similar during the upstroke and almost symmetric between the first half and the second half of the upstroke. Since pitching angular velocity  $\dot{\theta}$  (shown as a dashed line in Fig. 8) is positive in the first half and negative in the second half, the net power contribution of pitching motion is estimated to be near zero. However, at the high reduced frequency,  $f^* = 0.17$ , the peak of the pitching moment  $C_M(t^*)$  has shifted to the second half of the upstroke for all pitching amplitudes, and the magnitude of the peak increases when compared to the  $f^* = 0.09$  case. This asymmetric pitching moment results in negative net pitching power and pitching efficiency.

We can understand this by realizing that the dependence of the pitching moment on the reduced frequency is closely related to the growth of the leading-edge vortex. At the low reduced frequency,  $f^* = 0.09$ , the leading-edge vortex is already separated from the hydrofoil in the second half of the upstroke ( $t^* = 0.36$  in Fig. 8c). However, at the high reduced frequency,  $f^* = 0.17$ , the foil moves

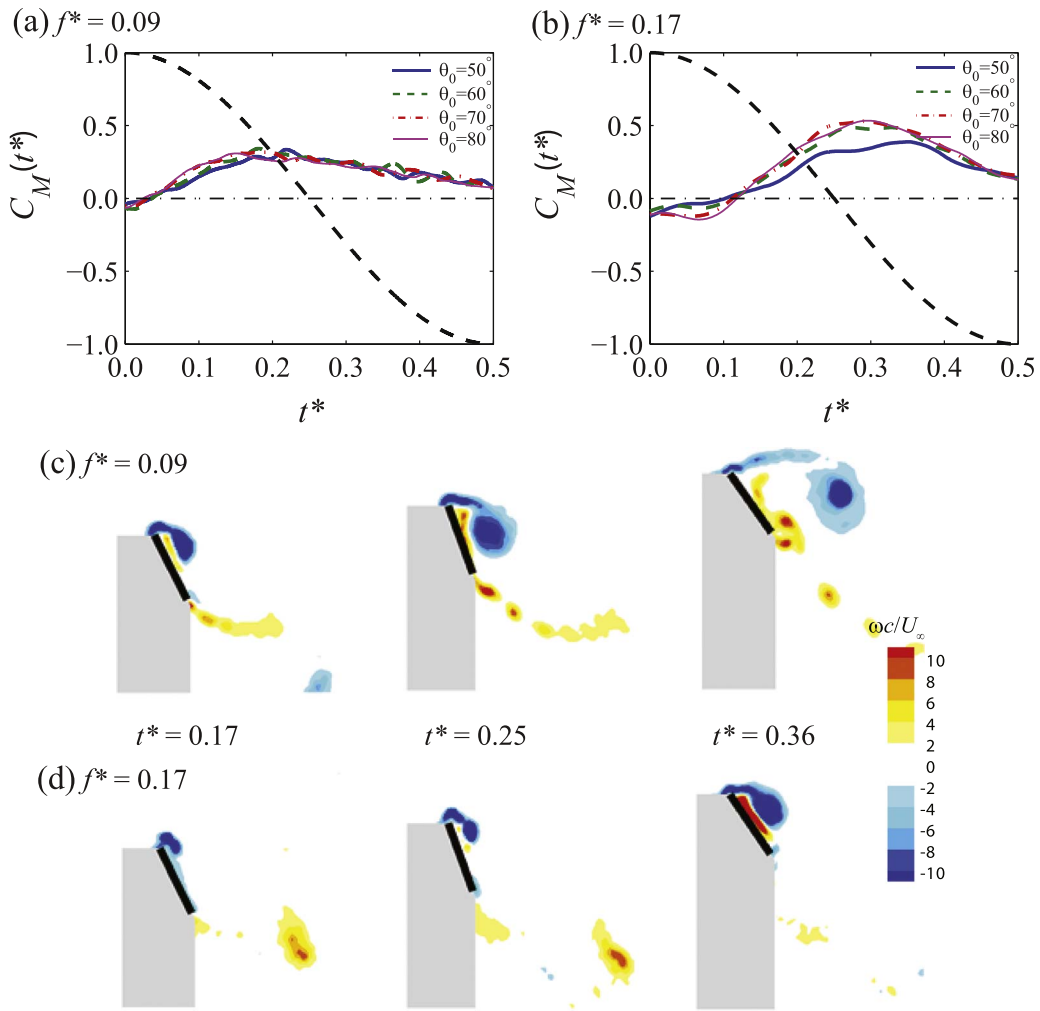


**Fig. 8.** (a,b) Pitching moment coefficient  $C_M$  during upstroke for four pitching amplitudes  $\theta_0 = 50^\circ - 80^\circ$  at (a)  $f^* = 0.09$  and (b)  $f^* = 0.17$ . Black dashed lines in (a) and (b) are pitching angular velocity normalized by maximum angular velocity ( $\dot{\theta}/\dot{\theta}_{max}$ ). (c,d) Sequences of leading-edge vortex dynamics during upstroke for  $\theta_0 = 70^\circ$  at (c)  $f^* = 0.09$  and (d)  $f^* = 0.17$ . The cross section of the hydrofoil is rectangular.

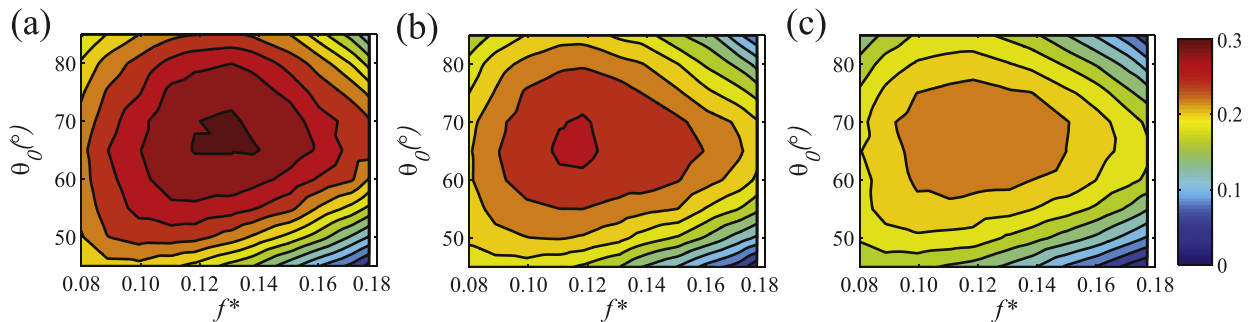


**Fig. 9.** Total efficiency  $\eta$  contours of the rectangular hydrofoil for three aspect ratios; (a)  $AR=4.5$ , (b)  $AR=3.5$ , and (c)  $AR=2.5$ .  $h_0^*$  is 0.8.

through the cycle faster, and the leading-edge vortex is still near the front part of the hydrofoil at  $t^* = 0.36$  (Fig. 8d). The size of the vortex in the  $f^* = 0.17$  case at  $t^* = 0.36$  is even smaller than that of the  $f^* = 0.09$  case at  $t^* = 0.25$ . The low pressure of the leading-edge vortex near the front part of the hydrofoil can induce a large positive pitching moment in the clockwise direction. Therefore, for a high reduced frequency, the pitching moment has a peak in the second half of the upstroke, which results in negative net pitching power over the stroke. It has been well known that the leading-edge vortex formation is critical in the performance of the hydrofoil (e.g. Zhu and Peng, 2009; Fenercioglu et al., 2015b). Our finding suggests that, by controlling the position and growth of the leading-

**Table 1**

Comparison of total efficiency  $\eta$  of the rectangular hydrofoil for the three aspect ratios without and with the end plates ( $\theta_0 = 70^\circ$  and  $f^* = 0.13$ ). The cross section of the hydrofoil is rectangular.

AR	No end plates	0.25c	0.50c	0.75c	1.00c
4.5	0.31	0.32	0.38	0.38	0.35
3.5	0.27	0.28	0.34	0.35	0.33
2.5	0.23	0.25	0.32	0.34	0.31

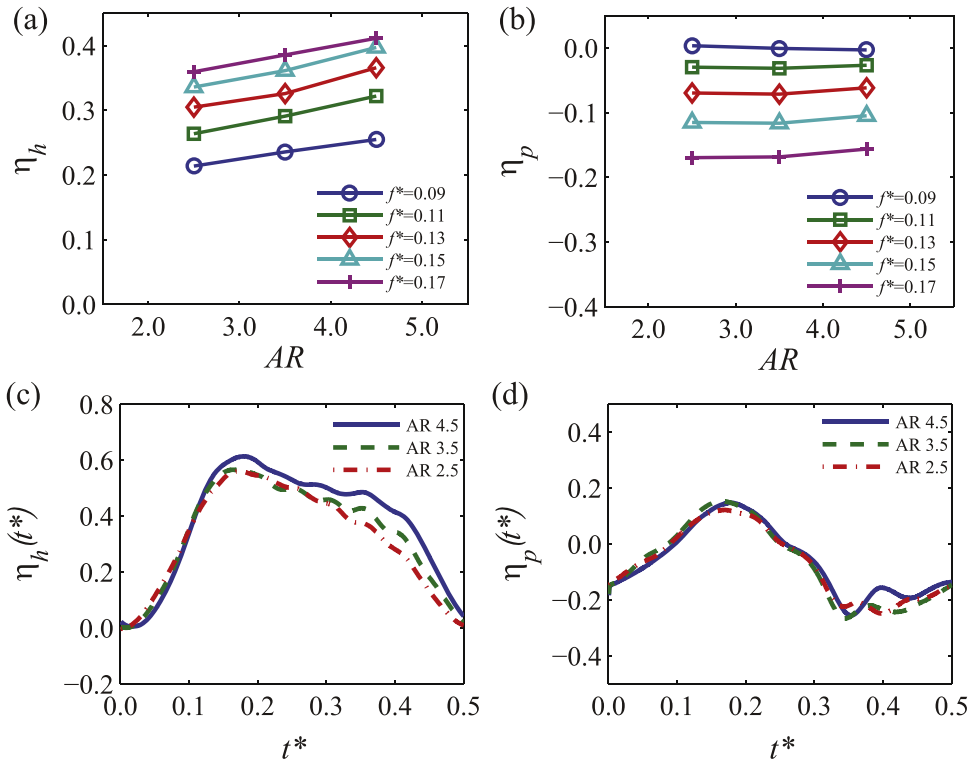


**Fig. 10.** (a) Efficiency by heaving  $\eta_h$  and (b) efficiency by pitching  $\eta_p$  as a function of  $AR$  for five reduced frequencies between  $f^* = 0.09$  and  $0.17$ ;  $\theta_0 = 70^\circ$  for (a) and (b). Time histories of (c) efficiency by heaving  $\eta_h(t^*)$  and (d) efficiency by pitching  $\eta_p(t^*)$  during upstroke for  $AR = 4.5, 3.5$  and  $2.5$ ;  $\theta_0 = 70^\circ$  and  $f^* = 0.13$ . The cross section of the hydrofoil is rectangular.

edge vortex, it may be possible to reduce the negative effect of the pitching motion on total efficiency.

**3.4. Effect of aspect ratio and end plates on efficiency**

Next, we consider the effects of the hydrofoil's aspect ratio and end-plate installation on efficiency for the hydrofoil with a rectangular cross section. Total efficiency  $\eta$  is compared for the three aspect ratios  $AR = 4.5, 3.5,$  and  $2.5$  in Fig. 9. Similarly to the previous computational work of Kinsey and Dumas (2012b), the total efficiency increases with  $AR$  over the whole parameter domain of  $\theta_0$  and  $f^*$  considered in this study. In the three  $AR$ s, the shapes of  $\eta$  contour levels do not change significantly even though the magnitudes of  $\eta$  are reduced for the small  $AR$ . The maximum  $\eta$  is at  $f^*=0.13$  and  $\theta_0 = 70$  for  $AR=4.5$ , and  $f^* = 0.12$  and  $\theta_0 = 65$  for both  $AR=3.5$  and  $2.5$ .

When the end plates shown in Fig. 2a are mounted, the total efficiency improves as the distance from the hydrofoil to the edge of the end plate  $d$  increases from  $0.25c$  to  $0.75c$  (Table 1). However, it decreases beyond  $d = 0.75c$ . In all three  $AR$ s, the maximum total efficiency is found at  $d = 0.75c$ . The reason for the efficiency reduction after  $d = 0.75c$  is not immediately apparent. The benefits of the end plates are usually thought to be the suppression of the tip vortex effects. However, skin friction on the end plates and interaction between the end plate and the flow structure may work against this benefit, reducing the hydrodynamic force on the hydrofoil. This balance appears to be favorable for small end plates but the costs outweigh the benefits in the case of the large end plate. Finding the optimal size of the end plate for efficiency improvement and elucidating the interaction of the end plate and the flow structure is one of the topics to investigate in future. Even though the end plate of  $d = 0.75c$  can remove three-dimensional flow near the tip, there is still some increase in the total efficiency with aspect ratio for  $d = 0.75c$ ; a similar result was reported in the simulation of Kinsey and Dumas (2012b).

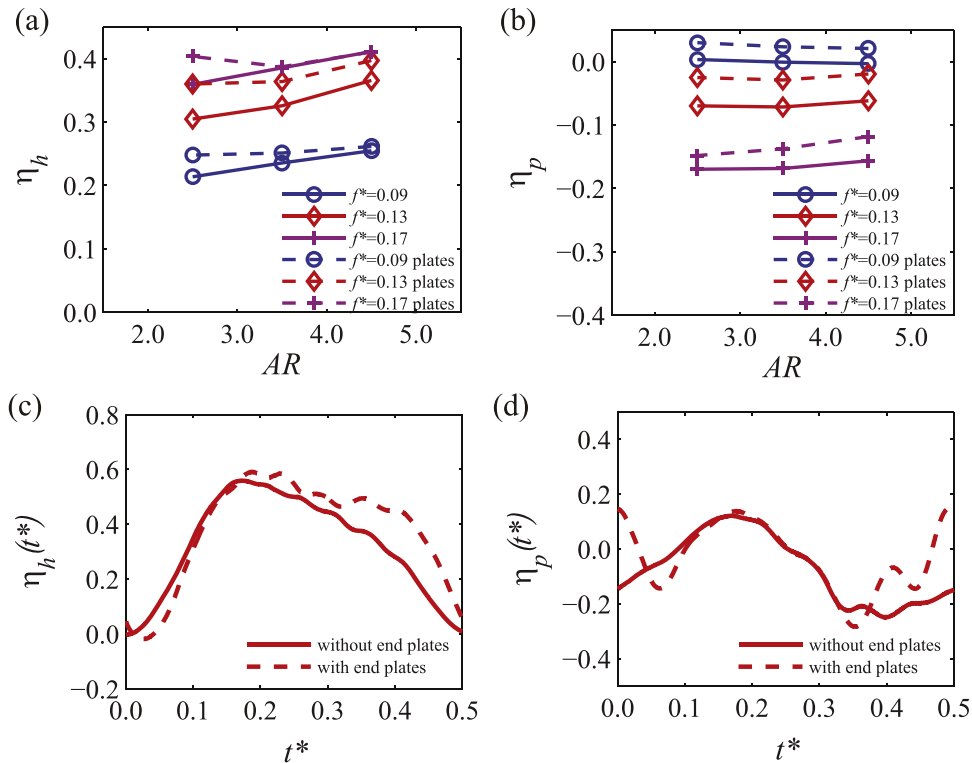


**Fig. 11.** Comparison of (a) efficiency contributed by heaving  $\eta_h$  and (b) efficiency contributed by pitching  $\eta_p$  between the rectangular hydrofoils without the end plates (solid lines) and with the end plates (dashed lines) for three reduced frequencies  $f^* = 0.09, 0.13,$  and  $0.17$ ;  $\theta_0 = 70^\circ$  for (a) and (b). Comparison of (c) efficiency by heaving  $\eta_h(t^*)$  and (d) efficiency by pitching  $\eta_p(t^*)$  time histories during upstroke;  $AR=2.5, \theta_0 = 70^\circ,$  and  $f^* = 0.13$ .

Heaving efficiency,  $\eta_h$ , and pitching efficiency,  $\eta_p$ , show different trends with the change in aspect ratio. They are compared for the three ARs in Fig. 10. In  $\theta_0 = 70^\circ$ ,  $\eta_h$  increases linearly with AR; the slope of the linear fitting curve  $\eta_h/AR$  is between 0.02 and 0.03 (Fig. 10a). This linear relationship may not be extended in the AR larger than 4.5 in that  $\eta_h$  should converge to an asymptotic value as AR becomes large. In steady airfoil theory, the tip vortex of the airfoil has a negative effect on the lift generation by reducing the effective angle of attack, and an airfoil with smaller aspect ratio generates a smaller lift force. A similar relationship can also be applied to the hydrofoil in heaving motion. However, during the early phase of the upstroke (or the downstroke), a vortex flow by the tip is only beginning to develop, and its effect is negligible. Therefore, the noticeable difference in the power by heaving motion among the three ARs is not observed at the early phase of the stroke (Fig. 10c). Instead, the difference among the three ARs is found at the middle and late phases of the stroke when the tip vortex has developed. Meanwhile, the pitching efficiency  $\eta_p$  is barely affected by the aspect ratio (Fig. 10b). The pitching efficiency is similar among the three ARs during the stroke although there is a minor difference in the late phase of the stroke (Fig. 10d). Most of the negative pitching power is generated in the second half of the stroke when the leading edge of the hydrofoil pitches against the free stream. Even though only the  $\theta_0 = 70^\circ$  cases are described in Fig. 10, the trends of Fig. 10 are generally found in other pitching amplitudes as well.

With the end plate of  $d = 0.75c$ , which is the most efficient end plate size according to Table 1, both  $\eta_h$  and  $\eta_p$  improve from the basic cases without the end plates for all  $f^*$  and  $\theta_0$  cases considered in this study. For clarity, only  $f^* = 0.09, 0.13,$  and  $0.17$  cases of  $\theta_0 = 70^\circ$  are shown in Figs. 11a and b. With the installation of the end plates, pitching efficiency  $\eta_p$  increases by similar magnitude, 0.02 – 0.04, for the three ARs. Meanwhile, the augmentation of heaving efficiency,  $\eta_h$ , by the end plates is affected by aspect ratio.  $\eta_h$  decreases with aspect ratio, and little improvement is observed in  $AR=4.5$ . The addition of end plates results in an increase in instantaneous heaving force and efficiency mainly in the second half of the upstroke (Fig. 11c). As explained above, the tip vortex has not developed at the early phase of the stroke and therefore, while the suppression of the tip vortex formation by the end plate has little influence on heaving force generation at the early phase, it has significant influence at the late phase. Therefore, the increase in heaving efficiency  $\eta_h$  by installing the end plates is sensitive to the aspect ratio. However, as can be seen in Fig. 10b and Fig. 11b, the pitching efficiency  $\eta_p$  is not strongly affected by the aspect ratio for both hydrofoil without the end plates and hydrofoil with the end plates. For the instantaneous pitching power, a large difference between the cases with and without the end plates is observed at the early and late phases of the upstroke when the pitch angle changes its sign (Fig. 11d). Pitching power for the case with the end plates can be positive near both  $t^* = 0$  and  $t^* = 0.5$ , during stroke reversal.

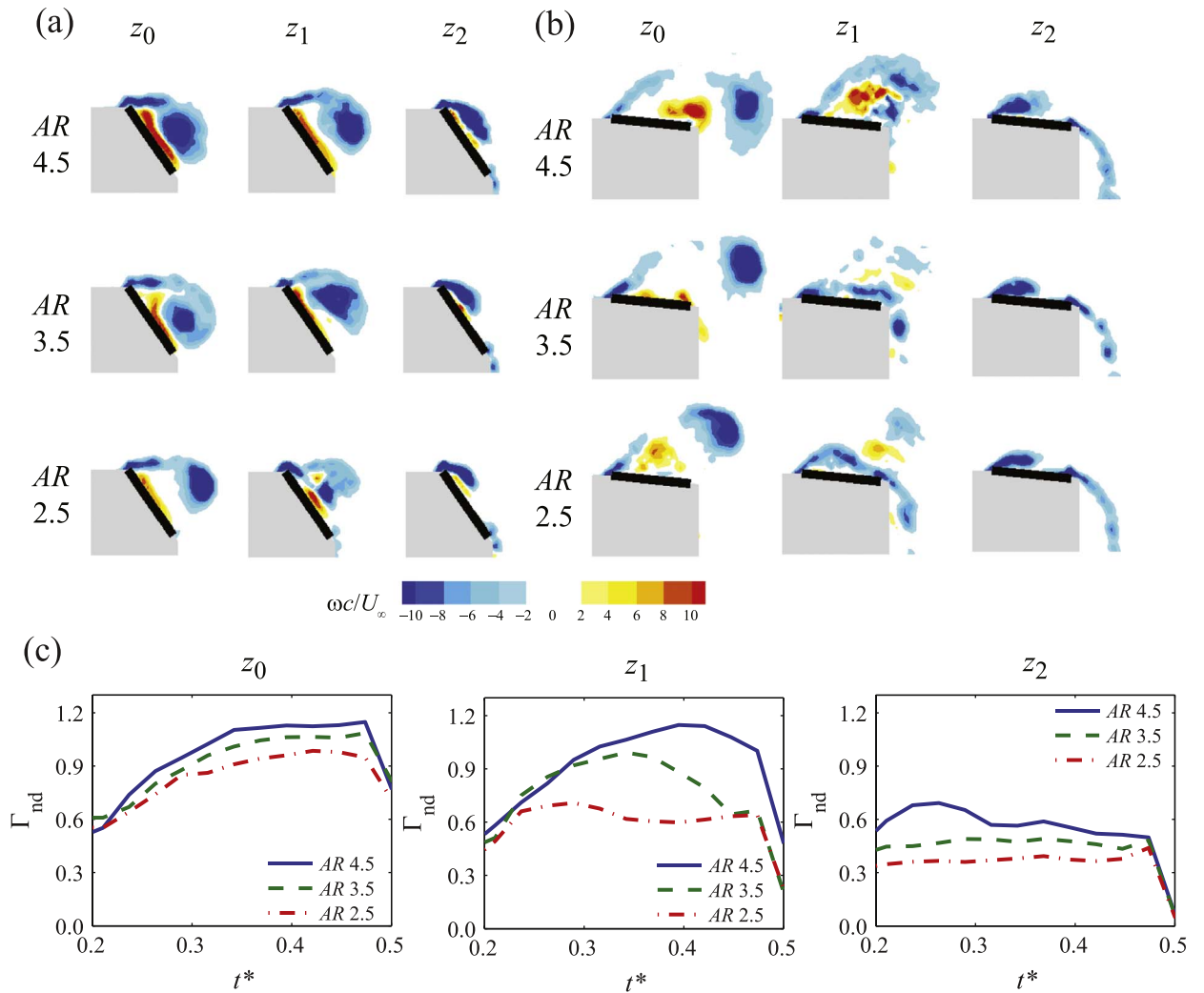


**Fig. 12.** Vorticity contours of the rectangular hydrofoil without end plates for the three aspect ratios at the three different spanwise sections ( $z = z_0, z_1, z_2$ ); (a) at about 3/4 of upstroke ( $t^* = 0.36$ ) and (b) near the end of upstroke ( $t^* = 0.49$ ). (c) Circulation  $\Gamma_{nd}$  of the leading-edge vortex during upstroke at the three spanwise sections. For these cases,  $\theta_0 = 70^\circ$  and  $f^* = 0.13$ .

### 3.5. Effect of aspect ratio and end plates on leading-edge vortex dynamics

At  $\theta_0 = 70^\circ$  and  $f^* = 0.13$  which are the optimal parameters for the  $AR=4.5$  case, the leading-edge vortex is compared for the rectangular hydrofoil of the three  $AR$ s in the three different spanwise sections  $z = z_0, z_1$ , and  $z_2$  defined in Fig. 2a (Figs. 12a and b). Note that, in our planar particle image velocimetry, only in-plane velocities were measured (and consequently only spanwise vorticity,  $\omega_z$ ), and there might be significant out-of-plane velocities, especially near the tip ( $z = z_2$ ), which we are not able to see. Nevertheless, it is clear that the development of the leading-edge vortex during the upstroke is suppressed near the tip for all three  $AR$ s as also observed in the computational work of Kinsey and Dumas (2012b). At about 3/4 of upstroke, the leading-edge vortex maintains a circular form at both  $z_0$  and  $z_1$  for  $AR=4.5$  and 3.5. However, the leading-edge vortex at  $z = z_2$  is stretched along the chord and remains close to the upper surface (Fig. 12a). For  $AR=2.5$ , the distance from the  $z = z_1$  section to the tip is closer than the other  $AR$ s and at this spanwise position the leading-edge vortex appears to be deformed by the strong influence of the tip vortex and it loses its circular core during the upstroke.

Near the end of the upstroke, the circular core of the leading-edge vortex moves farther from the hydrofoil in the section  $z_0$  (Fig. 12b). The counter-rotating vorticity (red contour in Fig. 12b) from the trailing-edge vortex rolls up above the hydrofoil in the section  $z_0$ . Meanwhile, in the section  $z_1$ , the leading-edge vortex loses its circular core due to its merging with the counter-rotating vorticity during pitch reversal (Fenercioglu et al., 2015b). In the section  $z_2$ , the leading-edge vortex is still close to the front part of the hydrofoil, and its growth is delayed.

In Fig. 12c, the strength of the leading-edge vortex as it develops during the upstroke is presented. In the definition of non-dimensional circulation  $\Gamma_{nd} = |\int \omega dA|/U_\infty c$ , only negative spanwise vorticity inside the leading-edge vortex was considered; the

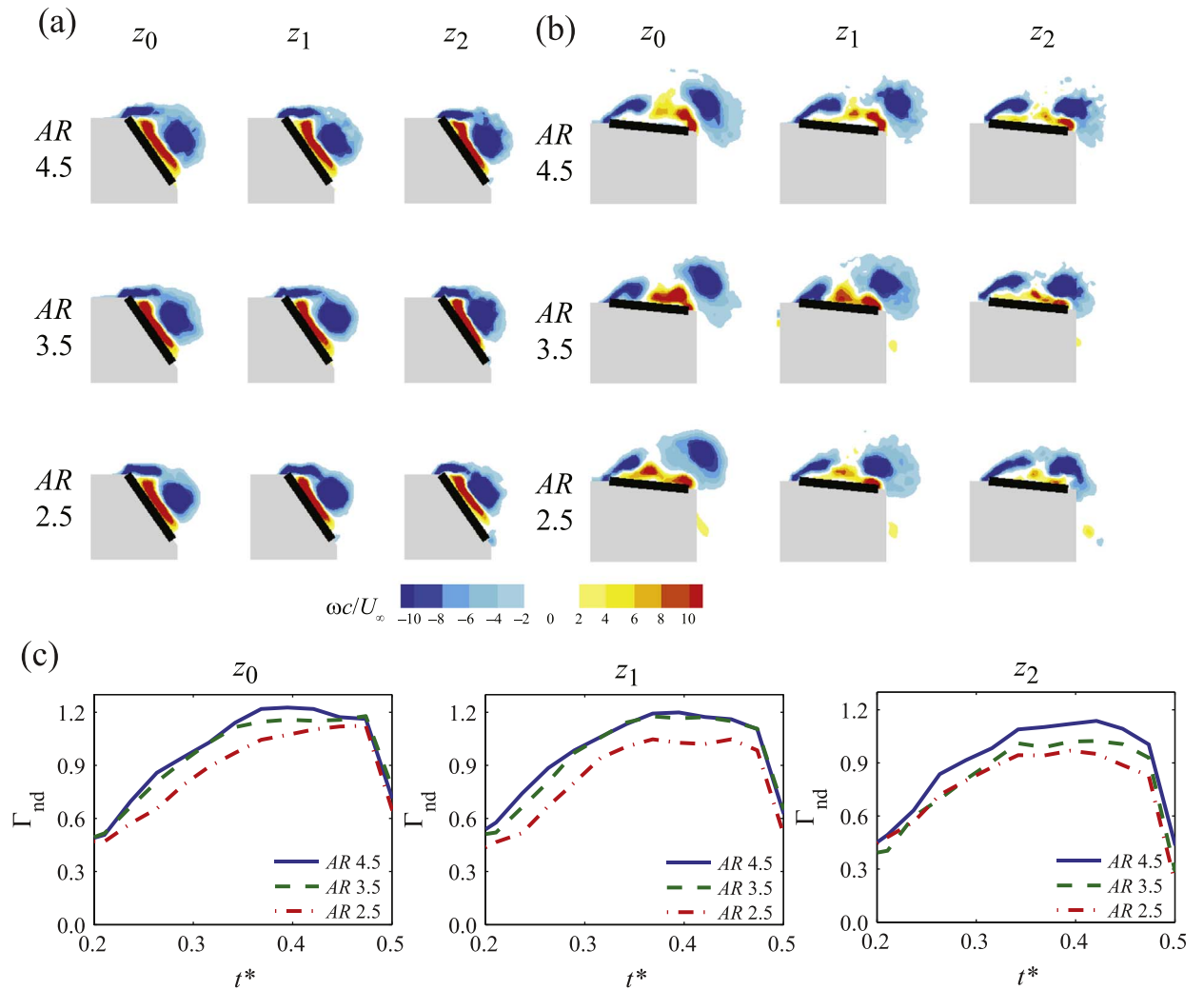


**Fig. 13.** Vorticity contours of the rectangular hydrofoil with end plates for the three aspect ratios at the three different spanwise sections ( $z = z_0, z_1, z_2$ ); (a) at about 3/4 of upstroke ( $t^* = 0.36$ ) and (b) near the end of upstroke ( $t^* = 0.49$ ). (c) Circulation  $\Gamma_{nd}$  of the leading-edge vortex during upstroke at the three spanwise sections. For these cases,  $\theta_0 = 70^\circ$  and  $f^* = 0.13$ .

threshold value of  $\omega c/U_\infty = -1$  was used in order to remove noise. According to Fig. 12c, the circulation of the leading-edge vortex becomes weaker nearer the hydrofoil tip. In the section  $z_0$ ,  $\Gamma_{nd}$  continues to increase until  $t^* = 0.45$ , but there is slight decrease of  $\Gamma_{nd}$  after  $t^* = 0.45$  because of the merging of the leading-edge vortex with the shedding counter-rotating vorticity. However, in the section  $z_2$ , the growth of the leading-edge vortex circulation is suppressed during the stroke and remains nearly constant during  $t^* = 0.20 - 0.45$ . At the sections  $z_0$  and  $z_2$ , even though there is difference in the magnitude of the leading-edge vortex circulation, the three AR cases show a similar trend. However, at the section  $z_1$ , while  $\Gamma_{nd}$  of the AR=4.5 case increases until  $t^* = 0.4$  similar to the section  $z_0$ ,  $\Gamma_{nd}$  of the AR=2.5 case has a plateau similar to the section  $z_2$ , which indicates that the suppression of the leading-edge vortex growth by the three-dimensional tip flow becomes effective for a larger portion of the span as the hydrofoil span (or AR) decreases. The reduced strength of the leading-edge vortex along the span for the small AR is correlated with the reduced heaving efficiency  $\eta_h$  in the small AR as mentioned in Section 3.4.

With the end plates, the size and position of the leading-edge vortex becomes more uniform at the three spanwise sections among the three ARs, as shown in Figs. 13a and b. The trend of the leading-edge vortex circulation also becomes similar among the three ARs;  $\Gamma_{nd}$  increases until  $t^* = 0.4$  and decreases near the end of the stroke (Fig. 13c). The slight difference in  $\Gamma_{nd}$  among the three ARs may be one of the reasons why  $\eta_h$  and  $\eta$  have some discrepancy among the three ARs with the end plates of  $d = 0.75c$  as shown in Table. 1. In Fig. 11d, it is demonstrated that pitching power for the hydrofoil with the end plates is positive near both  $t^* = 0$  and  $t^* = 0.5$ . With the installation of the end plate, the leading-edge vortex remains closely to the trailing edge of the hydrofoil during the stroke reversal while the leading-edge vortex is separated from the leading edge without the end plate. Compare Figs. 12b and 13b. Thus, during the stroke reversal, due to low pressure inside the leading-edge vortex, the pitching torque acts in the pitching direction; counter-clockwise direction in Figs. 12b and 13b. Since the magnitude of the pitching angular velocity is large during

stroke reversal, small pitching torque can produce large positive pitching power (Fig. 11d).

#### 4. Concluding remarks

In this paper, we have experimentally investigated the energy harvesting performance of the pitching and heaving hydrofoil with a focus on the effect of the hydrofoil shape and aspect ratio, and we analyzed the contribution from both heaving and pitching motions to the overall performance. The cross-section shape of the hydrofoil has little influence on the device performance for the shapes tested in this study, which is beneficial for the design of the hydrofoil. Rather than total efficiency, efficiency due to the heaving motion and efficiency due to the pitching motion show a better correlation with a pitching amplitude and a reduced frequency, and the competition between the two becomes clear. At a high reduced frequency, pitching power offsets large heaving power generation because of the slow formation of a leading-edge vortex and the resultant negative pitching power generated during pitch angle reversal. The control of the leading-edge vortex formation may be one of the approaches for the reduction of negative pitching power and the improvement of overall efficiency. While the efficiency due to pitching is hardly affected by the aspect ratio of the hydrofoil, the efficiency due to heaving varies linearly with the aspect ratios considered in this study. Both efficiency by heaving and efficiency by pitching improve by the installation of end plates. The effect of aspect ratio and end plates was also clearly observed in the formation of the leading-edge vortex during a stroke.

This work was funded by the US Department of Energy, ARPA-e (DE-AR0000318). DK also received support from the Basic Science Research Program through the National Research Foundation of Korea (NRF) funded by the Ministry of Science, ICT & Future Planning (NRF-2015R1C1A1A02037111).

#### References

- Ashraf, M.A., Young, J., La, J.C.S., Platzer, M.F., 2011. Numerical analysis of an oscillating-wing wind and hydropower generator. *AIAA J.* 49, 1374–1386.
- Birnbaum, W., 1924. Das ebene problem des schlagenden flügels. *Z. Ange. Math. Mech.* 4, 277–292.
- Ellington, C.P., vandenBerg, C., Willmott, A.P., Thomas, A.L.R., 1996. Leading-edge vortices in insect flight. *Nature* 384, 626–630.
- Fenercioglu, I., Zaloglu, B., Ashraf, M.A., Young, J., Lai, J.C.S., Platzer, M.F., 2015a. Flow around an oscillating tandem-wing power generator. In: 53rd AIAA Aerospace Sciences Meeting, AIAA 2015-1751. Kissimmee, FL.
- Fenercioglu, I., Zaloglu, B., Young, J., Ashraf, M.A., Lai, J.C.S., Platzer, M.F., 2015b. Flow structures around an oscillating-wing power generator. *AIAA J.* 53, 3316–3326.
- Franck, J., Breuer, K., Fawzi, A., Cardona, J., Miller, M., Su, Y., Medina, A., Loera, C. L., Junquera, E., Simeski, F., Volkman, K., Lorick, R., Cowles, S., Ribeiro, B. L. R., Winckler, S., Derektor, T., Mandre, S., 2015. Oscillating hydrofoils for tidal energy extraction: experiments, simulations and salt water field tests. In: American Geophysical Union, Fall Meeting. San Francisco, CA.
- Jones, K.D., Platzer, M.F., 1997. Numerical computation of flapping-wing propulsion and power extraction. In: 35th Aerospace Sciences Meeting & Exhibit, AIAA 97-0826. Reno, NV.
- Karakas, F., Fenercioglu, I., 2016. Effect of phase angle on tandem flapping wing power generation. In: 2nd International conference on energy production and management in the 21st century, Ancona, Italy.
- Karakas, F., Zaloglu, B., Fenercioglu, I., Hoke, C., Young, J., Lai, J., Platzer, M., 2016. On optimal oscillating-foil power generation in free and constrained flow. In: 54th AIAA Aerospace Sciences Meeting, AIAA 2016-2070, San Diego, CA.
- Kinsey, T., Dumas, G., 2008. Parametric study of an oscillating airfoil in a power-extraction regime. *AIAA J.* 46, 1318–1330.
- Kinsey, T., Dumas, G., 2012a. Optimal tandem configuration for oscillating-foils hydrokinetic turbine. *J. Fluids Eng.* 134, 031103.
- Kinsey, T., Dumas, G., 2012b. Three-dimensional effects on an oscillating-foil hydrokinetic turbine. *J. Fluids Eng.* 134, 071105.
- Kinsey, T., Dumas, G., Lalande, G., Ruel, J., Mehut, A., Viarouge, P., Lemay, J., Jean, Y., 2011. Prototype testing of a hydrokinetic turbine based on oscillating hydrofoils. *Renew. Energy* 36, 1710–1718.
- Le, T.Q., Ko, J.H., Byun, D., 2013. Morphological effect of a scallop shell on a flapping-type tidal stream generator. *Bioinspir. Biomim.* 8, 036009.
- Liu, W.D., Xiao, Q., Cheng, F., 2013. A bio-inspired study on tidal energy extraction with flexible flapping wings. *Bioinspir. Biomim.* 8, 036011.
- Maxworthy, T., 1979. Experiments on the weis-fogh mechanism of lift generation by insects in hovering flight. 1. Dynamics of the fling. *J. Fluid Mech.* 93, 47–63.
- McKinney, W., DeLaurier, J., 1981. Wingmill: an oscillating-wing windmill. *J. Energy* 5, 109–115.
- Platzer, M. F., Sarigul-Klijn, N., Young, J., Ashraf, M. A., Lai, J.C.S., 2011. Renewable hydrogen production using sailing ships. In: ASME International Mechanical Engineering Congress & Exposition, IMECE2011-62311, Denver, CO.
- Semler, C.S., 2010. Experimental investigation on an oscillating flow generator. M.S. thesis Naval Postgraduate School.
- Simpson, B. J., Licht, S., Hover, F., Triantafyllou, M.S., 2008. Energy extraction through flapping foils. In: Proceedings of the 27th International Conference on Offshore Mechanics and Arctic Engineering, Estoril, Portugal.
- Usoh, C.O., 2015. Numerical study of a flapping flat plate for power generation. Ph.D. thesis University of New South Wales.
- Usoh, C.O., Lai, J., Ashraf, M., 2012. Numerical analysis of a non-profiled plate for flapping wing turbines. In: The 18th Australasian Fluid Mechanics Conference. Launceston, Australia.
- Wu, J., Qiu, Y.L., Shu, C., Zhao, N., 2014. Pitching-motion-activated flapping foil near solid walls for power extraction: a numerical investigation. *Phys. Fluids* 26, 083601.
- Wu, J., Shu, C., Zhao, N., Tian, F.-B., 2015. Numerical study on the power extraction performance of a flapping foil with a flexible tail. *Phys. Fluids* 27, 013602.
- Xiao, Q., Liao, W., Yang, S.C., Peng, Y., 2012. How motion trajectory affects energy extraction performance of a biomimetic energy generator with an oscillating foil? *Renew. Energy* 37, 61–75.
- Xiao, Q., Zhu, Q., 2014. A review on flow energy harvesters based on flapping foils. *J. Fluids Struct.* 46, 174–191.
- Young, J., Ashraf, M.A., Lai, J.C.S., Platzer, M.F., 2013. Numerical simulation of fully passive flapping foil power generation. *AIAA J.* 51, 2727–2739.
- Young, J., Lai, J.C., Platzer, M.F., 2014. A review of progress and challenges in flapping foil power generation. *Prog. Aerosp. Sci.* 67, 2–28.
- Zhu, Q., 2011. Optimal frequency for flow energy harvesting of a flapping foil. *J. Fluid Mech.* 675, 495–517.
- Zhu, Q., Peng, Z., 2009. Mode coupling and flow energy harvesting by a flapping foil. *Phys. Fluids* 21, 033601.